

GEOMETRIC RETRIEVAL OF CLOUD TOP HEIGHT FROM MISR IMAGERY

Jia Zong

Jet Propulsion Laboratory, California Institute of Technology

Mail Stop 169-315

4800 Oak Grove Drive

Pasadena, CA 91109 USA

ABSTRACT

The Multi-angle Imaging SpectroRadiometer (MISR) instrument for the Earth Observing System (EOS) is to be launched in 1999 aboard the EOS AM-1 satellite. The MISR instrument consists of nine pushbroom cameras pointing at discrete view angles. Multi-angle imagery from MISR creates opportunities to retrieve new scientific parameters relating to the earth's aerosols, clouds, and surface. This paper focuses on the accurate geometric retrieval of cloud top height from MISR data. It consists of three major processing steps. The first process projects and registers multi-angle MISR radiance imagery to an ellipsoidal earth surface represented by the WGS-84 ellipsoid. The result of this processing provides not only surface registration but also near epipolar imaging geometry. The next processing step separates the cloud motion and cloud height. Traditionally, this has been considered a singular problem in photogrammetry even with stereo imagery. However, a separation condition does exist with satellite imaging and multiple MISR camera look-angles. The last processing step automatically retrieves cloud-top height field in high resolution from ellipsoid-projected MISR radiance imagery. This paper presents the above three processing steps starting from an accurate and efficient projection of multi-angle MISR image data to the ellipsoid surface, followed by a mathematical derivation which separates the cloud motion and height, and finally an automatic image matching and ray intersection algorithm for high resolution cloud top height retrieval.

Key Words: Image registration, epipolar geometry, image matching, cloud motion, cloud height.

1. INTRODUCTION

The Multi-angle Imaging SpectroRadiometer (MISR) instrument for the Earth Observing System (EOS) is to be launched in 1999 aboard the EOS AM-1 satellite [Diner, et. al.1991]. It consists of nine pushbroom cameras pointing at discrete view angles of 0° , $\pm 26.1^\circ$, $\pm 45.6^\circ$, $\pm 60.0^\circ$, and $\pm 70.5^\circ$ with respect to the earth surface. The cameras are designated as An for nadir, Af, Bf, Cf, Df for the forward set and Aa, Ba, Ca, Da for the aftward set of cameras, respectively. Each camera is equipped with four Charge-Coupled Device (CCD) line arrays filtered to provide one of MISR spectral bands (centered at 446, 558, 672, and 866 nm). Each line array consists of 1504 photoactive pixels. The cross-track instantaneous field of view and sample spacing is 275 m for off-nadir cameras and 250 m for the nadir camera. The along-track sample spacing is always 275 m while instantaneous field of views vary and may overlap depending on camera view angle. The satellite flies in a sun-synchronous 705 km descending polar orbit, and is capable of global coverage every nine days. It takes about 7 minutes for the MISR instrument to observe any ground region with all nine cameras.

The purpose of the MISR instrument is to study the ecology and climate of the earth through the acquisition of systematic, global multi-angle imagery in reflected sunlight. Routine science data processing of MISR images will be conducted at the NASA Langley Distributed Active Archive Center (DAAC). The data reduction process is required to be autonomous and continuous in order to provide data of science value for long term monitoring and allowing intercomparison with other data sources. Through Level 1 standard processing, MISR raw instrument data are both radiometrically and geometrically corrected. The subsequent Level 2 science processing derives geophysical parameters such as aerosol optical depth, cloud classification matrices, and albedos. One of the science objectives in the Level 2 Top of Atmosphere (TOA) cloud processing is to determine cloud classification and spectral albedos at a reflecting level reference altitude (RLRA). The RLRA is defined to be the level found by matching features (or areas) with the greatest contrast in the near-nadir viewing directions. Physically, this corresponds to the main reflecting layer, which will typically be the tops of bright clouds, or the surface for clear scenes.

Stereoscopic retrieval of image features has been commonly recognized as an accurate autonomous data detection technique in the remote sensing and photogrammetry communities. The approach involves automatic image matching from stereo images and surface reconstruction from conjugate look rays which generally leads to a digital elevation model (DEM) as an output

product. Nevertheless, stereoscopic retrieval of cloud top height has not yet been as successful because not only does it require stereo images in epipolar or near epipolar geometry to ensure the success and efficiency of image matching; it also easily results a singular condition in the inverse process of ray intersection when cloud motion is present. Multi-angle imagery from MISR creates opportunities to retrieve cloud top height stereoscopically on a global basis. In addition, the multiple views from satellite altitude over a wide angular range also separates the effect of wind displacement independently from height. The essentials of geometrical reduction of cloud top height from MISR imagery are a) geo-registration and rectification of MISR imagery in Level 1 processing, which prepares for the stereo retrieval of cloud top height, b) geometric separability of disparities due to cloud motion and height, and c) automatic matching of cloud features with greatest contrast and construction of the RLRA field. This paper presents the underlying principle of the algorithm and prototype results with simulated test data.

2. MISR SURFACE ELLIPSOID REGISTRATION

There are several reasons to project MISR image data to an ellipsoid surface on a global basis. First, the TOA cloud retrievals are required to be derived from multi-angle MISR image data at known geographical locations. Second, the construction of RLRA on a global basis from stereo disparities favors a smooth and analytical base surface. Third, stereo image matching processing can be much more efficient with image data rectified in epipolar or near epipolar geometry. The physical MISR instrument has 2800 km maximum instantaneous displacement in the along-track direction, as shown in Figure 1.a. In order to geolocate and co-register MISR images for stereo processing, we choose to project all 36 channels of MISR image data from nine camera view angles to the WGS84 ellipsoid surface. The Space-Oblique Mercator (SOM) map projection is used for the georegistration. As illustrated in Figure 1.b, the radiometrically corrected and georectified radiance product after Level 1 processing represents a continuously superimposed set of multi-angle multi-spectral data. In an abstract world, the ellipsoid-projected radiance may be looked upon as the data collected by a “virtual” MISR. Theoretically, ground features at the zero elevation relative to the WGS84 ellipsoid have no image disparity in the ellipsoid radiance product.

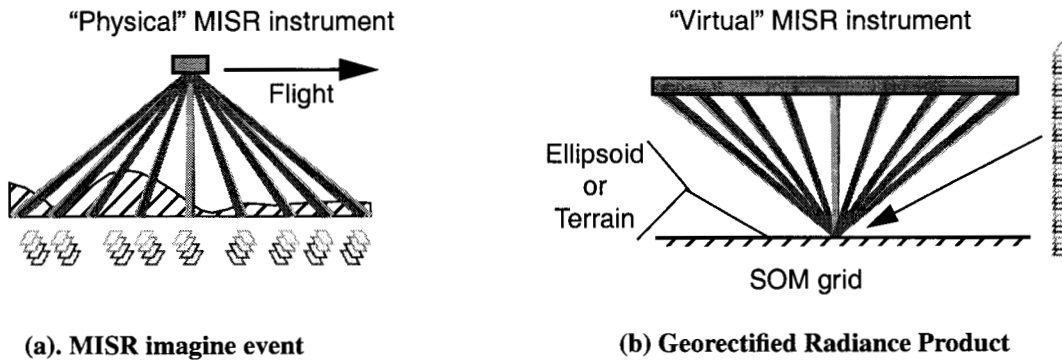


Figure 1: MISR imaging and geometric process

2.1. Ellipsoid Projection Algorithm

The projection from MISR instrument data to ellipsoid surface is required to be not only accurate but also autonomous and continuous. Ignoring dynamic errors in the reported navigation data, the algorithm relies on a transformation which maps the local ellipsoid surface represented with SOM directly to the MISR image space. The relationship between MISR image coordinates and the analytically defined ellipsoid surface is modeled focusing on the following four elements: 1) the satellite orbit, 2) the camera geometry, 3) earth rotation, and 4) the ellipsoid curvature. Figure 2 shows the Df camera image locations of four sparse SOM lines evenly distributed over a segment of 70.4 km MISR ground track. The deformation of SOM lines in image space is to be modeled by the ellipsoid transform.

One ellipsoid transform is independently derived and applied to each of the 36 channels of MISR imagery. Each transform applies to a segment of a SOM swath and links the predefined SOM grids with one band of MISR data. Not only is backward projection from the ellipsoid surface to image space efficient, it can also easily use image coordinate corrections (ICC) to

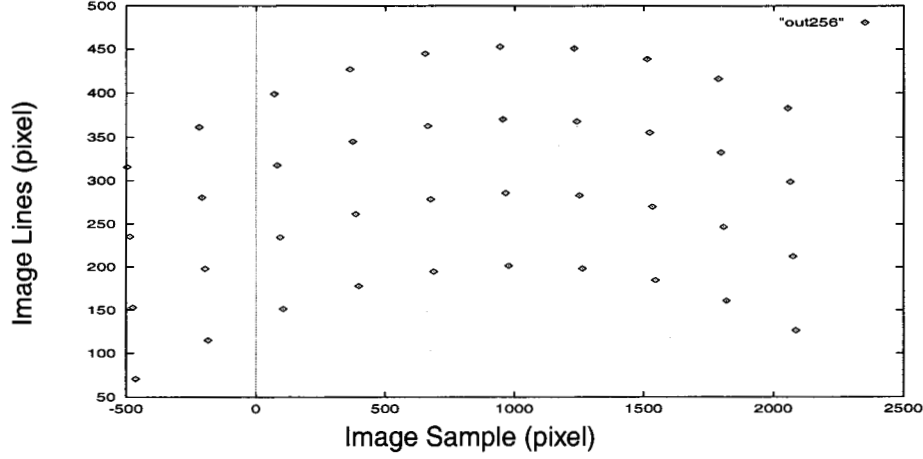


Figure 2: Df image location of sparse SOM grid centers

improve the projection accuracy. ICC is determined from a parallel process which projects MISR instrument data to the topographical surface, see [Jovanovic, et. al. 1996]). It represents corrections to static errors in the image coordinates resulting from errors in the navigation data. In addition, the resampled image has higher accuracy and better quality without having to smooth any missing points as would be the case in a forward intersection approach. The ellipsoid projection algorithm consists of the following components:

1) Tie-point Determination: A number of tie-points are first selected for building the transform. Tie-points are evenly spaced throughout the predefined SOM segment while the transform is built. All tie-points have zero elevation relative to the WGS84 ellipsoid. The SOM coordinates of the tie-points will be used to build the transform.

2) Backward Projection: Backward intersection is performed to determine the MISR image coordinates of the tie-points. The underlying principle of backward projection is the collinearity equation that converts look vectors from ground space to image space. Root finding is required for the pushbroom cameras to determine the image time, and make use of navigation data. See [Jovanovic, et. al. 1996] for details.

3) Image Coordinate Correction: Image coordinates are modified using the ICC obtained from the projection of MISR image to topographical surface. This corrects for static errors in the backward intersection.

4) Build Ellipsoid Transform: Estimate transform parameters using tie-points, see section §2.2.

5) Apply Ellipsoid Transform: At every 275 m SOM map grid, apply ellipsoid transform to determine its image coordinate.

6) Resample MISR image: Bilinearly resample the radiometrically corrected radiance data to the ellipsoid surface at 275 m SOM map grids.

2.2. Ellipsoid Transform

Assuming a perfect pin-hole camera and a planar ground surface, the mapping of any line on this plane surface in the image space will also be a straight line. This can be written by an affine transform:

$$l_{img} = c_1 + c_2 \Delta l_{som} + c_3 \Delta s_{som} \quad (1)$$

$$s_{img} = d_1 + d_2 \Delta l_{som} + d_3 \Delta s_{som} \quad (2)$$

Where l_{img} and s_{img} are image line and sample coordinates, $\Delta l_{som} = l_{som} - (l_{som})_0$ and $\Delta s_{som} = s_{som} - (s_{som})_0$ are SOM grid indices relative to a center location assuming no distortion over SOM space.

Replacing the straight line on the above planar surface with a curve over a cylinder, results in a non-linear mapping of this line from SOM space to image space. Figure 3 illustrates the conversion of an arc distance over a circle to chord distance on a plane. Let A be the center position of SOM area, C be the arc distance over the circle representing Δs_{som} and s be the corresponding chord distance on the plane P , we have the following relation:

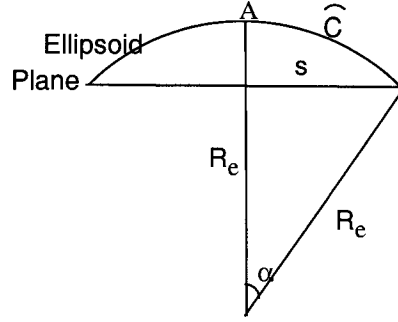


Figure 3: Relationship of line distance and arc distance

$$s = R_e \sin \frac{C}{R_e} \quad (3)$$

The relative sample distance in Eq. (1) and (2) should be substituted with Eq. (3) to correct for the curvature effect across the swath. Since MISR camera are not perfect pin-holes and the swath direction is varying as earth rotates, we want to expand Eq. (3) to a Taylor series as $s = k_1 C + k_3 C^3 + O(C^5)$. Now we have the mapping from SOM to image space:

$$l_{img} = c_1 + c_2 \Delta l_{som} + c_3 \Delta s_{som} + c_4 \Delta s_{som}^3 \quad (4)$$

$$s_{img} = d_1 + d_2 \Delta l_{som} + d_3 \Delta s_{som} + d_4 \Delta s_{som}^3 \quad (5)$$

For a short segment of SOM swath, the ellipsoid surface is also curved in the along-track direction. Replacing the cylinder surface with an ellipsoid surface, the ellipsoid curvature affects not only along the sample direction but also along the radial direction of a point to the center of swath, as seen in Figure 4. Therefore we replace the sample term in the

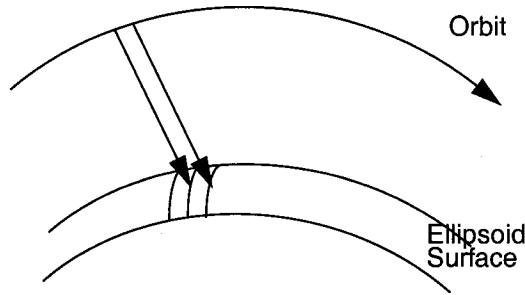


Figure 4: Mapping of multiple lines along the swath

previous equation with the radial distances Δr , where $\Delta r^2 = \Delta l_{som}^2 + \Delta s_{som}^2 + 2\Delta l_{som}\Delta s_{som}$. If a set of transforms applies only to limited lines in the along-track direction, we can ignore the higher order terms of Δl_{som} and update the mapping function with two additional terms:

$$l_{img} = c_1 + c_2\Delta l_{som} + c_3\Delta s_{som} + c_4\Delta s_{som}^2 + c_5\Delta l\Delta s + c_6\Delta s_{som}^3 \quad (6)$$

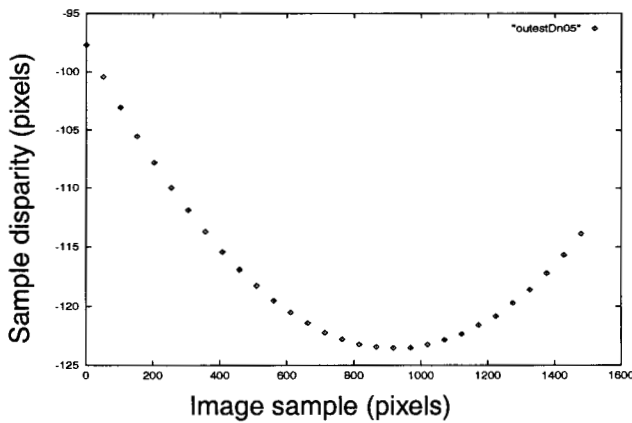
$$s_{img} = d_1 + d_2\Delta l_{som} + d_3\Delta s_{som} + d_4\Delta s_{som}^2 + d_5\Delta l\Delta s + d_6\Delta s_{som}^3 \quad (7)$$

By incorporating the curvature factor along the swath we are able to apply a transform to a segment of swath instead of a line. Here, all the four factors in the mapping from image to ellipsoid surface affect how many additional terms should be added in the mapping transform, and for what distance along the swath that a set of transform coefficients can be applied. First, the ellipsoid transform is dynamically calculated on-the-fly to take into account orbit perturbations and navigation errors. Its application range depends closely on the dynamic portion of navigation error. We set it to be compatible with the application range of a set of ICC parameters. Second, the effects of MISR camera along-track and side-looking angles are included in the above transform. The effect of focal length variation should be smaller than the navigation error variation. Third, earth rotation causes SOM swath to change its direction which also limits the application range of the ellipsoid transform, though we found this to be a relatively minor factor. Finally, as elaborated above, the ellipsoid curvature is the major contributor to the higher order sample terms and the cross terms in Eq. (6) and (7). By limiting the application range along the swath, we can ignore higher order terms other than those presented in Eq. (6) and (7).

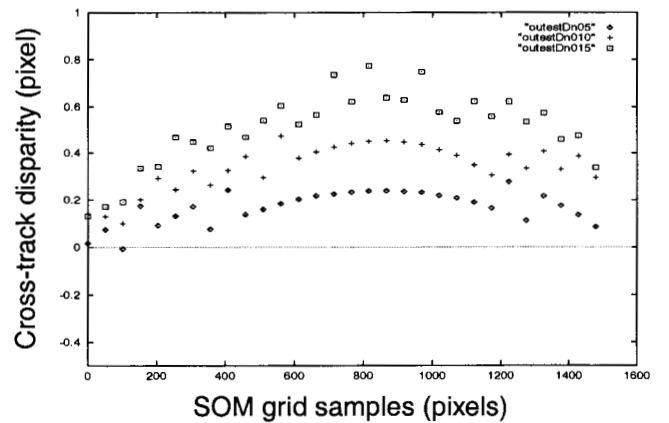
The ellipsoid transform coefficients are calculated by a least-squares fitting procedure using the corresponding image and SOM coordinates of the tie-points. The transform will then be used to resample the current channel image radiances onto all 275 m SOM grids for the segment.

2.3. Epipolar Nature of Ellipsoid Projected Radiance Imagery

A pair of stereo images can be considered in epipolar geometry when they are leveled at the same elevation, and rotated to normal vertical attitude. Theoretically a true epipolar condition only exists for center perspective images. Epipolar images contain no y-parallax making image matching relatively efficient and feasible since only one-dimensional searching of conjugated image features is needed. Rectifying MISR imagery to the zero elevation ellipsoid surface creates a very similar effect. That is, all MISR images are leveled at the same elevation surface. The difference of the camera side-looking angles for any pair of MISR cameras causes little or no cross-track image disparity, even for images at the very edges of the MISR swath. Figure 5.a



(a) Misr D camera image sample disparity.



(b) D camera cross-track disparity of clouds at 5, 10, 15 km above WG84 ellipsoid after projection.

Figure 5: Sample disparity in MISR image and surface ellipsoid.

depicts the sample disparities of one MISR image line for the D camera assuming the elevations of the image line are zero relative to the WGS84 ellipsoid. The sample deformation of image lines from one camera to another is corrected after the ellipsoid projection. Figure 5.b shows the sample disparities of cloud spots on the SOM map grids at 5, 10, and 15 km above the WGS84 ellipsoid for the same D camera pair. The cross-track disparities are less than 1 pixel. These figures are created using simulated ellipsoid projected MISR imagery [Lewicki, et. al. 1994].

3. SEPARATE CLOUD MOTION FROM HEIGHT

The key to stereoscopic retrieval of an object surface is to determine heights from image disparities. By definition, an object feature has image disparity when observed from two different angles. Physically, disparity is caused by a height difference of an object feature from a fixed point plus any motion of the object along the direction where the disparity is measured. In our case, a cloud above the ellipsoid surface causes an image disparity shown in Figure 6 as $\overline{AB_1}$, where A and B_1 represent the conjugate image features of a cloud edge. In the absence of cloud motion, the cloud height can be obtained from intersecting conjugate look rays \vec{a} and $\vec{b_1}$. If the cloud also has a velocity component along the flight direction, the disparity $\overline{AB_2}$ is then caused by the combined effect from both the cloud height and the cloud motion. Direct intersecting look rays \vec{a} and $\vec{b_2}$ would result in an incorrect cloud height h' . In order to obtain accurate values of cloud top height, it is necessary to separate the disparities due to cloud advection from those due to cloud height.

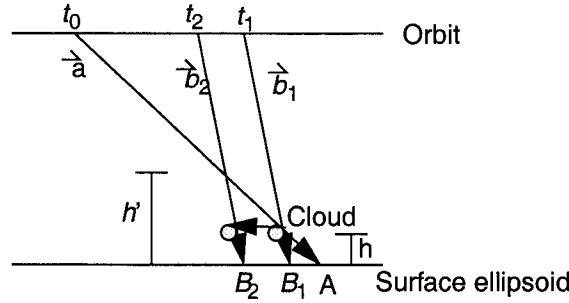


Figure 6: Disparity of cloud edge in two images with different view angles

3.1. Separation Condition

Figure 7 shows the geometry of MISR imaging in the along-track direction where cloud height and motion are highly correlated due to large view angle difference from one camera to another. The shaded circles indicate the locations of a cloud at times t_i , assuming a constant along-track cloud motion v_c . The projections of the cloud onto the surface ellipsoid are at the locations x_i at these times, with the discrete MISR camera view angles θ_i . For simplicity in this discussion, the cloud motion and the camera look vectors are assumed to lie in the along-track plane. Letting a cloud edge been seen by two cameras with different view angles at times t_1 and t_2 , respectively, the following equations represent the traveling distances of the spacecraft and that of the cloud during this time interval:

$$v_s(t_2 - t_1) = (R + H)(\alpha_2 - \alpha_1) - (R + H)(\Gamma_2 - \Gamma_1) \quad (8)$$

$$v_c(t_2 - t_1) = (R + h)(\alpha_2 - \alpha_1) - (R + h)(\gamma_2 - \gamma_1) \quad (9)$$

where v_s and v_c are the velocities of the spacecraft and the cloud in the along-track direction, respectively, R is the radius of the Earth, H is the orbit altitude above the Earth's surface, and h is the cloud height. As shown in Figure 7, α_1 and α_2 are the angles between the initial radial line at time t_0 and the radial line passing the image locations x_1 and x_2 , respectively; Γ_1 and Γ_2 are the angles between the radial lines to the spacecraft and the corresponding image locations x_1 and x_2 ; and γ_1 and γ_2 are the angles between the radial lines to the cloud and the corresponding image locations x_1 and x_2 . Since $h \ll R$, Eq. (9) can be rewritten with variables that we are interested in:

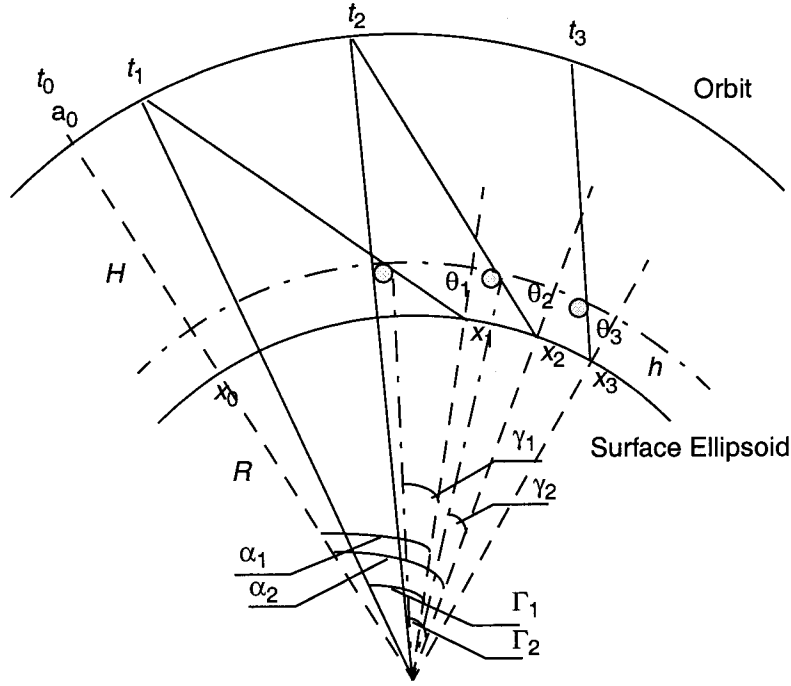


Figure 7: Geometry of MISR imaging of cloud in the along-track direction

$$v_c(t_2 - t_1) = (x_2 - x_1) + h(\tan\theta_1 - \tan\theta_2) \quad (10)$$

With multi-angle images, Eq. (10) can be generalized into a linear system as follows:

$$v_c(t_j - t_i) - h(\tan\theta_i - \tan\theta_j) = (x_j - x_i) \quad (11)$$

$(i, j = 1, 2, \dots, n, i \neq j, n \geq 3)$

The linear system expressed by Eq. (11) represents a straight line in the Δx versus Δt space in which each matching pair contributes a point to this line, where v_c and h can be determined from the slope and intercept of the line. Matching at least three images with different view angles θ_i are required to solve for v_c and h . In addition, any two linear equations are dependent on each other if their determinant is zero, i.e., if

$$\det A = (t_i - t_{i-1})(\tan\theta_i - \tan\theta_{i+1}) - (t_{i+1} - t_i)(\tan\theta_{i-1} - \tan\theta_i) = 0 \quad (12)$$

In such a case, v_c and h are inseparable from these two equations. On a small scale where the flight line is straight and the surface is a plane, this singularity will always be true. On an orbital scale with a circular or an elliptic orbit and a spheroidal or an ellipsoidal surface, the traveling time interval between a pair of cameras does not linearly relate to the tangent of view angles as depicted in Figure 7 and represented in Eq. (8), as long as the selected camera view angles do not happen to be symmetric around the nadir view.

3.2. Cloud Motion and Height Retrieval

Having proven cloud motion and height separation condition in one-dimension, we describe the three-dimensional cloud motion field retrieval algorithm in this section. In MISR processing, we assume that vertical cloud motion can be ignored dur-

ing the 7 minute time interval between camera Df and Da views, and that the horizontal cloud motion at a given altitude is constant during this period of time over a domain size of ~ 100 km. In order to determine a regional cloud motion field, a feature-based matching algorithm is used to simultaneously retrieve velocity and height values for a sparse subset of conjugate features in the MISR imagery. The algorithm is first applied to the Df, Bf, and An cameras to detect the image disparity values [Diner, et. al. 1997]. The cloud height and motion of each point from this subset is determined by intersecting the three-dimensional conjugate look rays obtained from image matching. The algorithm is applied independently to the Da, Ba, and An cameras. The results are combined to generate the final cloud motion field.

Assume that there is no vertical cloud motion but only a constant horizontal cloud motion. The cloud motion vector, the conjugate look rays from image matching of D, B, and An cameras, and the surface disparities resulting from the matching should form a closed loop in a three-dimensional Cartesian coordinate system as shown in Figure 8. The following vector equations represent this relationship:

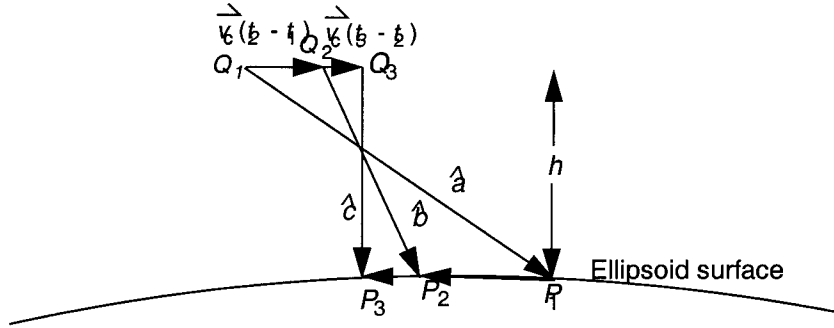


Figure 8: Ray intersection to retrieve cloud motion

$$\overrightarrow{P_1 P_2} = \lambda_2 \hat{b} + \vec{v}_c(t_2 - t_1) - \lambda_1 \hat{a} \quad (13)$$

$$\overrightarrow{P_2 P_3} = \lambda_3 \hat{c} + \vec{v}_c(t_3 - t_2) - \lambda_1 \hat{b} \quad (14)$$

where \vec{v}_c is the unknown cloud motion velocity; P_1 , P_2 , and P_3 are the three-dimensional ground points obtained from image matching, representing conjugate image locations of the same cloud edge on the ellipsoid surface; \hat{a} , \hat{b} , and \hat{c} are the known unit vectors of the conjugate look rays; and λ_1 , λ_2 , and λ_3 are the unknown scale factors of the look rays for them to intersect with the cloud, respectively. We now represent the above relationship in a local coordinate system such that its z-axis is aligned with the zenith direction at nadir image point P_3 . The x-axis and the y-axis are aligned with the along-track and cross-track directions, respectively. The condition of no vertical cloud motion $v_{cz} = 0$ can be easily imposed. The remaining unknowns, the horizontal cloud motion (v_{cx} , v_{cy}) and the ray vector scale factors (λ_1 , λ_2 , λ_3) can be solved simultaneously with the above six equations for each set of 3 conjugate look rays. The cloud top height of this matched triplet is obtained by projecting the nadir view look ray, e.g. $\lambda_3 \hat{c}$, onto the normal direction at the ellipsoid surface where the look ray intersects:

$$h = \lambda_3 \hat{c} \cdot \hat{n} \quad (15)$$

4. CLOUD TOP HEIGHT RETRIEVAL

Cloud motion is typically homogeneous over a larger area than cloud height. Once the regional motion field has been derived, it serves to provide a cloud motion correction in the conversion of the fine resolution disparities to heights. The high resolution image disparity field is derived with combined feature-based and area-based matching algorithms applied to two pairs of near-nadir cameras (Af-An and Aa-An). The matching scheme is designed to be both accurate and efficient, for details see [Diner, et. al. 1997]. The search window of conjugate cloud features is limited to a narrow band aligned with the along-track direction

and is affected by three factors: a) ellipsoid projected radiance imagery is in near epipolar geometry as illustrated in section §2.3; b) camera along-track angles and maximum cloud top height define a maximum along-track search range; and c) the cloud motion field in both along-track and cross-track directions are known from the previous process. The cloud top height retrieval from conjugate image rays is constructed with a modified version of the minimum distance intersection to be discussed in this section. The resulting cloud height retrieval (based on Af-An and Aa-An results) is used to establish the RLRA.

Ray intersection with minimum distance intersection is a simple algorithm. As shown in Figure 9.a, it considers the errors associated with camera look rays and errors introduced during the processing of image co-registration and image matching, and determines the minimum distance vector \hat{d} between two conjugate look rays \hat{a} and \hat{b} as:

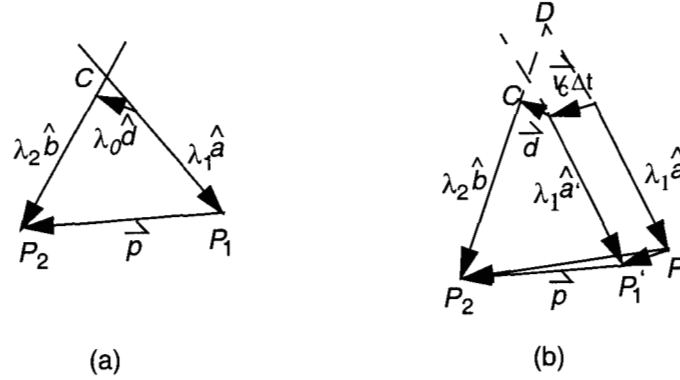


Figure 9: Minimum distance of conjugate rays with and without motion

$$\hat{d} = \hat{a} \times \hat{b} \quad (16)$$

If \hat{p} denotes the vector connecting the two ground points P_1 and P_2 on the surface ellipsoid from image matching, then the four vectors \hat{p} , $\lambda_2 \hat{b}$, $\lambda_1 \hat{a}$, and $\lambda_0 \hat{d}$ must close, where λ_0 , λ_1 , and λ_2 are the scale factors to the corresponding vectors. Now consider a cloud moving with velocity \vec{v}_c (horizontally in two dimensions) during the period Δt between the conjugate cloud features that were seen by the two involved cameras. As shown in Figure 9.b, \hat{a}' is the look vector as if there is no cloud motion, and \hat{a} is the real look vector due to the existence of cloud motion $\vec{v}_c \Delta t$. If we directly intersect the two look vectors \hat{a} and \hat{b} , the intersection will be around point D at a wrong height. To remove the cloud motion effect, we assume the cloud was actually seen by another look vector \hat{a}' parallel to \hat{a} at another ground position P_1' by the forward camera A at the time t_p . The corrected vector equation can be represented as:

$$\hat{p} - \vec{v}_c \Delta t = \lambda_2 \hat{b} + \lambda_0 \hat{a}' - \lambda_1 \hat{a} \quad (17)$$

Eq. (17) contains 3 individual equations and 3 unknowns λ_0 , λ_2 , λ_3 for each pair of conjugate rays. The intersecting cloud top location can be obtained starting from the nadir image location, i.e. P_2 :

$$C = P_2 - \lambda_2 \hat{b} - \frac{1}{2} \lambda_0 \hat{a} \quad (18)$$

5. ALGORITHM TEST RESULT

The Level 1 standard processing of ellipsoid projection of MISR imagery has been implemented and tested with simulated MISR image data. The MISR imagery simulation was based on Landsat Thematic Mapper (TM) data, along with a registered DEM. The simulation process is described in [Lewicki, et. al. 1994]. The accuracy of ellipsoid projection depends closely on

the dynamic errors presented in the navigation data. According to reports on the stability of the EOS-AM platform, the predicted behavior is substantially better than the requirement. At 95% confidence level, the ellipsoid projection errors are 1.5 pixels in along-track direction and 0.5 pixels in cross-track direction using orbit data simulated according to the stability requirement, or 0.6 pixels in along-track direction and 0.5 pixels in cross-track direction using orbit data confined to the worst case predicted orbit performance.

A Prototype test algorithm has been implemented to examine the epipolar nature of ellipsoid projected radiance imagery. Simulated cloud locations are sparsely distributed over the MISR swath at various elevations. One of the test results has been provided in Figure 5. The test demonstrated up to one pixel cross-track displacement for cloud up to 20 km above the WGS84 ellipsoid.

Another prototype algorithm was implemented to prove the separability of cloud motion and height with MISR data. The cloud features were simulated with velocity at 0, 12, 24, or 48 m/s in any horizontal direction. In Table 1, column one lists the MISR camera triplet used for simultaneous cloud motion and height retrieval. The determinants of these camera combination according to Eq. (12) are in column two. The cloud motion and height retrieval are listed in the remaining columns. σ_{diff} represents the standard deviation of the retrieval from the known value. Max_{diff} is the largest error observed. For asymmetric camera combinations An-Bf-Df and Aa-Bf-Df, the maximum cloud motion deviation is less than 1 m/s from the true value and maximum cloud top height deviation is less than 60 m. On the other hand, for symmetric camera triplets An-Bf-Aa and An-Bf-Aa, their determinants are too close to zero to provide reliable retrievals. The test confirmed our selection of the D, B, and An camera triplets for the stereoscopic retrieval of cloud motion. In case any default camera does not provide good image data, an alternative camera set that passes the determinant test will be used.

Table 1: Cloud Motion Retrieval Test Results

Camera Triplet	$detA$ (line)	Δv_{cx} (m/s)		Δv_{cy} (m/s)		Δh (m)	
		σ_{diff}	Max_{diff}	σ_{diff}	Max_{diff}	σ_{diff}	Max_{diff}
An-Bf-Df	-1229.7	0.35	0.89	0.03	0.08	22.1	53.5
Aa-Bf-Df	-1891.6	0.36	0.88	0.03	0.09	26.0	60.8
An-Bf-Aa	-40.7	0.92	2.96	0.15	0.49	84.5	268.0
An-Bf-Ba	-6.1	12.2	36.5	1.72	5.08	1102.9	3284.5

6. SUMMARY

Using a backward projection transform, we have projected and co-registered MISR radiance data from all nine cameras to a reference ellipsoid surface defined at the WGS84 ellipsoid. The ellipsoid projected radiance imagery has been proven to be in near epipolar geometry which serves for the stereoscopic retrieval of cloud top height. By using non-symmetric MISR cameras, including the most oblique ones, we are able to avoid mathematical singularity and obtain an accurate retrieval of regional cloud motion fields. Finally, fine resolution cloud top heights on a global basis can be retrieved stereoscopically using ellipsoid-projected MISR radiance imagery after correction for the regional cloud motion field.

7. ACKNOWLEDGMENTS

The author gratefully acknowledges the efforts of David J. Diner, Roger Davies, John V. Martonchik, and Jan-Peter Muller of the MISR Science Team, and Graham W. Bothwell, Earl G. Hansen, Veljko M. Jovanovic, Scott A. Lewicki, and Michael M. Smyth of the MISR Science Data System Team. This research is being carried out at the Jet Propulsion Laboratory, California Institute of Technology, under contract with the National Aeronautics and Space Administration.

8. REFERENCES

- Diner, D. J., Bruegge, C. J., Martonchick, J. V., Bothwell, G. W., Danielson, E. D., Floyd, E. L., Ford, V. G., Hovland, L. E., Jones, K. L., and White, M. L., A Multiangle Imaging SpectroRadiometer for Terrestrial Remote Sensing from the Earth Observing System, International Journal of Imaging Systems and Tech, vol.3, pp. 92~109, 1991
- Diner, D. J., Davies, R., Di Girolamo, L., Horvath, A., Moroney, C., Muller, J-P., Paradise, S. R., Wenkert, D., Zong, J., Level 2 Cloud Detection and Classification Algorithm Theoretical Basis, JPL internal document D-11399, Rev. C, 1997
- Jovanovic, V. M., Smyth, M. M., and Zong, J., Autonomous and Continuous Georectification of Multi-angle Imaging Spectro-Radiometer (MISR) Imagery, ISPRS Int. Arch. of Photogrammetry, vol. XVIII, Commission II, pp. 176~181, Vienna, 1996
- Lewicki, S. A., Smyth, M. M., Jovanovic, V. M., and Hansen, E. G., A Simulation of EOS MISR Data and Geometric Processing for the Prototyping of the MISR Ground Data System, IGARSS, vol III, pp. 1543~1545, Pasadena, CA 1994